Distribution of Active Faults and Lithospheric Discontinuities in the Himalayan-Tibetan Orogenic Zone Identified by Multiscale Gravity Analysis

X. L. Wu[1*] and J. F. Wu[1]

[1]School of Geomatics, Xi'an University of Science and Technology, Xi'an, China.

Corresponding author: X. L. Wu (xlong_wu@126.com)

Abstract

To reveal the spatial distribution of major active faults and structural discontinuities in the Himalayan-Tibetan orogen, this paper presents wavelet multiscale analysis of the Bouguer gravity field and solves the total horizontal derivatives of each wavelet detail. The results show that, in general, the crustal discontinuities on the Pamir Plateau and in the Himalayan tectonic zone are significant. On the northern margin of Tibet, active faults are mostly visible only in the deep crust. In eastern Tibet, crustal discontinuities decrease as depth increases. The Himalayan crust is undergoing E-W extension, and material discontinuities are significant along N-S-trending normal faults. The Sangri-Nacuo fault is the tectonic boundary between the Himalayan tectonic zone and the eastern Himalayan syntaxis and cuts off the entire lithosphere of Tibet. The spatial structural distributions of the western and eastern Himalayan syntaxes are very different. The former is relatively intact and extends deeper in the lithosphere, while the latter is more complex and shallower than the Mohorovicic discontinuity, and its overlying crust has deformed intensely from the collision between the Indian and Eurasian plates. Further, the structural distribution in the upper mantle reveals that the wedging Indian plate in the western Himalayan syntaxis almost reaches the SW margin of the Tarim basin and forms a closed structure in western Tibet, which could help to explain the eastward extrusion of the Tibetan Plateau.

1 Introduction

The Himalayan-Tibetan orogen is the primary part of the intercontinental deformation zone in the India-Eurasia collision system. It is composed of the Tibetan Plateau and the Pamir Plateau. The former is the youngest plateau in the world, while the latter exhibits geodynamic processes comparable to those of the Tibetan Plateau (Li et al. 2008; Bhatti et al. 2018; Burtman and Molnar 1993; Schwab et al.2004; Burtman 2013; Pan et al.2018; Wu et al.2020). The Cenozoic tectonic evolutionary processes and kinematic characteristics of the Himalayan-Tibetan orogenic zone are mostly expressed by the development of complex fault systems, folds and blocks (Li et al. 2020. Dong et al. 2020; Gao et al. 2020; Yang et al. 2020; Zhang et al. 2016; Liang et al. 2013; Li et al. 2018; Ansberque et al. 2018; Wang et al. 2001; Chen et al. 2004). How these structures accommodate the convergence between the Indian and Eurasian plates is the key to revealing both the collisional process between the two plates and the mechanisms of tectonic evolution (Ge et al. 2015; Holt et al. 1995, 2000; England et al. 1986). There is long-term controversy regarding the roles of active faults in the process of tectonic evolution. Some scholars argue that active faults are very important because they separate the crust into a series of rigid blocks, and crustal deformation of the study area is mainly accommodated by activity along these major faults (Molnar et al. 1975, 1984; Tapponnier et al. 1982; Chung et al. 1997). Others argue that the principal characteristics of crustal deformation in the study area are continuous and widely diffused. Active faults have a very limited role in adjusting the process of present-day crustal deformation

(England and Mckenzie,1982; England and Molnar, 1990; Vilotte et al. 1982; Houseman and England, 1986; 1993). Therefore, the detailed spatial distribution of active faults and structural discontinuities in the lithosphere is the key to understanding the role of active faults in the process of regional crustal deformation and tectonic evolution.

The Bouguer gravity anomaly is the superimposed effect of all geologic elements with different scales, densities and depths (Li W., 2019). Because of the very limited extents of active faults within the lithosphere, we utilized the wavelet multiscale decomposition technique to distinguish the contributions of gravitational sources at different depths (Yang et al. 2001; Xu et al. 2015) and then calculated the total horizontal derivative (THD) on each wavelet transform detail to reveal the spatial distributions of active faults and structural discontinuities at different depths in the study area.

2 Bouguer gravity anomalies at different depths

Based on the free-air gravity anomaly provided by Sandwell et al. (2014), we utilized the FA2BOUG program (Fullea et al. 2008) to obtain the Bouguer gravity anomaly of the study area. Thus, to reveal the characteristics of the gravity field and infer the corresponding tectonic features at different depths in the study area, we performed a 7th-order wavelet decomposition on the Bouguer gravity anomalies using a biorthogonal 3.1 wavelet (bior3.1) and then evaluated the field source depth using the radial power spectrum algorithm. Further, we established the spherical MQ model (Hardy,1976) on each wavelet detail and solved the THD, which has a higher accuracy than the VDR (vertical derivative) method when dealing with the potential field on grid points (Wang et al. 2009). To facilitate the understanding of the relationships between the tectonic setting and lithospheric discontinuities, we present an active tectonic map (Figure 1) of the study area based on the studies of Taylor and Yin (2009), Deng et al. (2007) and Schurr et al. (2014). The wavelet decompositions of Bouguer gravity anomalies are shown in Figure 2, and the corresponding field source depths are listed in Table 1.

Figure 1. Major active faults related to the Himalayan-Tibetan orogenic zone (**Strike-slip faults:** ATF, Altyn Tagh fault; AplF, Apalong fault; AnhF, Anninghe fault; BtF, Batang fault; CF, Chaman fault; DlsF, Daliangshan fault; GlgF, Gaoligong fault; HF, Herat fault; HyF, Haiyuan fault; JsjF, Jinshajiang fault; JlF, Jiali fault; TF, Talas-Fergana fault; KKF, Karakash fault; KF, Karakorum fault; KYS, Kashgar-Yecheng transfer system; LGF, Longmu-Gongzha fault; NjF, Nujiang fault; NthF, Nantinghe fault; SF, Sagaing fault; SKF, Sarez-Karakul fault; XshF, Xianshuihe fault; YnxF, Yunongxi fault. **Thrust faults and fold-thrust belts:** BFB, Burmese fold belt; LmsT, Longmenshan thrust; MCT, Main Central thrust; MFT, Main Frontal thrust; PTS, Pamir thrust system; QNT, Qilian Nanshan thrust; SMTS, Sarez Murghab thrust system; STT, Southern Tianshan Thrust; TTS, Tanymas thrust system. **Normal faults and extensional structures:** ALAF, Alucuo-Lamucuo-Aguocuo fault; CPF, Cangmucuo-Palongcuo fault; GM, Gurla-Mandhata detachment; SDGF, Shuangban-Dangruoyongcuo-Gucuo fault; SNF, Sangri-Nacuo fault; YGF, Yadong-Gulu fault; XSDF, Xiangcuo-Shenzha-Dingjie fault. **Suture zones:** AMS, Anyimaqen-Kunlun-Muztagh suture zone; BNS, Bangonghu-Nujiang suture zone; JS, Jinsha suture zone; RE, Rushan-Pshart suture zone; SSZ, Shyok suture zone; YZYS, Yalu-Zangbo suture zone.)

As shown in Figure 2, the 1st- to 5th-order wavelet details (Figure 2(a) to Figure 2(e)) clearly reflect the tectonic boundaries of the orogenic zone. The Bouguer gravity anomalies of the Pamir Plateau, Tian Shan range and tectonic boundaries of the Tibetan Plateau are relatively complex.

Positive and negative anomalies are alternately distributed and reflect evident features of the tectonic boundaries that separate the Himalayan-Tibetan orogenic zone from its surrounding structures. Such complexity is mainly related to the uneven density of the upper crust. As the depth of the field source increases, under intense tectonic activity, widespread metamorphism occurs in the sedimentary structures. Therefore, the complex gradient belts of Bouguer gravity anomalies tend to connect into larger pieces, and the complexity of the Bouguer gravity anomalies is reduced. At a depth of 17 km (Figure 2(e)), the anomalies show a regular distribution between positive values and negative values, which is obviously related to the spatial distributions of major active faults exposed at the Earth's surface. The elongated belts of high positive gravity anomalies are distributed along the MFT (main frontal thrust), ATF (Altyn Tagh fault) and KKF (Karakash fault) on the southern and northern margins of Tibet.

The spatial distribution characteristics of Bouguer gravity anomalies change significantly when the depth increases further, and the structural configurations become more indistinct. In Figure 2(f), corresponding to the bottom of the crust, the negative anomalies are mostly distributed at the eastern and western ends of the Tibetan Plateau, such as the MFT near the WHS (western Himalayan syntaxis), the KKF and ATF of northwestern Tibet, the southern segment of the YGF (Yadong-Gulu fault) and JlF (Jiali fault), and the NjF (Nujiang fault) and BFB (Burmese fold belt) near the EHS (eastern Himalayan syntaxis). Negative anomalies distributed along the YGF, southern BFB and NjF appear from the shallow crust to the deep crust. The volcanic rocks distributed in the shallower crust could not form such spatial patterns. This indicates that the negative anomalies mostly result from crustal stacking or folding of the Mohorovicic discontinuity. In addition, in the mid-Himalayas between 75°E and 90°E, the anomalies are close to zero, whereas the BNS (Bangong Nujiang suture zone) and its northern lithosphere exhibit significant positive anomalies. This pattern indicates the existence of a broken subducted or subducting plate.

Compared with the overlying crust, the materials are obviously redistributed and readjusted at a depth of 136 km in Figure 2(g). The Bouguer gravity anomalies are significantly related to the spatial distributions of major active structures. There are two significant positive gravity anomalies in the study area. One corresponds to the Tarim basin, and the other corresponds to the Indian plate close to the WHS that forms an evident wedging feature. The northern boundary of the latter is the SSZ (Shyok suture zone), and its western boundary is highly in accordance with the CF (Chaman fault) and Quetta valley. The CF is widely recognized as a tectonic boundary between the Indian plate and Eurasian plate in this region. These two positive regions seem to collide with each other, and the NW-SE gradient belt of negative gravity anomalies between them is intensely squeezed. This negative anomaly continuously covers the entire Pamir, western Tian Shan and western Tibet. In the Tian Shan range, this negative gradient belt is cut off by the TF (Talas-Fergana fault), and in Tibet, it tends in the direction of the KF (Karakoram fault), which separates the Pamir Plateau and Tibetan Plateau structurally. Farther east, this negative gradient belt is divided into two narrower belts, the YZYS (Yalu-Zangbo suture zone) and western JS (Jinsha suture zone). In addition, the Shan Plateau and Sichuan-Yunnan tectonic zone show significant negative Bouguer gravity anomalies. Near the EHS, the positive anomalies form a narrow belt distributed along the JlF, NjF and BFB, and the southern end of the YGF also exhibits significant positive anomalies.

Figure 2(h) shows the wavelet approximation of the entire study area, which relates to the material distribution in the deep Earth. Compared with those in the overlying lithosphere, the significant negative Bouguer gravity anomalies further tend to the northeast, and the negative gravity anomalies of the NW Pamir and Himalayan tectonic zones are close to zero. This reveals that crustal and mantle materials are squeezed into the Tarim basin and northern Sichuan-Yunnan

tectonic zone, where the characteristics of negative anomalies are evident.

Figure 2. Wavelet decomposition of Bouguer gravity anomalies. (a)~(g) are the 1st- to 7th-order wavelet transform details. (h) is the 7th-order wavelet approximation.

Table 1. The estimates of approximate field source depths

Number of order	1	2	3	4	5	6	7
Field depth (km)	0.5	2.5	6.5	10	17	85	136

3 Edge recognition on wavelet transform details

Discontinuities in lithospheric materials and active fault distributions at different depths can be clearly recognized by the maximum values of the THDs. In Figure 3, the THD values of the boundary zone between the Indian plate and Eurasian plate are higher than those of the northern crust. On the Pamir Plateau, the maximum values are mainly distributed along its boundary structures, such as the KYS (Kashgarr-Yeshgar transfer system), KF, SSZ and western segment of the PTS (Pamir thrust system). The global maximum values are mostly located in front of the Nanga-Parbat of the WHS. In addition, the Pamir Plateau can be divided into two subunits by the N-S-trending Sarez-Karakul fault (SKF). In the western Pamir, the maximum values are more obvious than those in the east, which indicates that the crust in the western Pamir is much more broken than the eastern crust. On the Tibetan Plateau, the maximum THD values are mainly distributed within the Himalayan tectonic zone south of the KF and YZYS. The THD values over the GM (Gurla-Mandhata detachment) and along a series of N-S-trending normal faults, such as the SDGF (Shuangban Dangxiong Gucuo fault), XSDF (Xiangcuo Shenzha Dingjie fault), and SNF (Sangri-Nacuo fault), are much higher than those of the crust of the immediate neighborhood. On the eastern boundary of the Tibetan Plateau, the intersection position of the AplF (Apalong fault) and JlF in the EHS as well as the NjF and XshF (Xian Shui He fault) and the intersection position between the AnhF (An-Ning-He fault) and DlsF (Daliangshan fault) also exhibit evident material discontinuities, which indicate the presence of structural discontinuities along the abovementioned structures.

Figure 3. Distributions of the total horizontal derivatives at 0.5 km depth

In Figure 4, the discontinuities along the QNT (Qilian-Nanshan fault) on the northeastern margin of the Tibetan Plateau appear, which are not evident in the shallower crust. In the western Pamir, the maximum values of THDs become more significant and widespread, whereas the tectonic discontinuities between the Pamir Plateau and the Tarim basin are evident because the maximum values of THDs along the KYS are significant. On the Tibetan Plateau, the structural discontinuities along the mid-Himalayan rise as well as the maximum values of THDs are still concentrated on the GM and N-S normal faults. On the eastern boundary of the Tibetan Plateau, crustal discontinuities along the JlF between the YZYS and AplF (Apalong fault) are significant. In addition, the NjF, JsjF (Jinshajiang fault), YnxF (Yunongxi fault), AnhF, XshF and LmsT (Longmenshan thrust) become more evident than they are in the shallower crust.

Figure 4. Distributions of the total horizontal derivatives at 2.5 km depth

In Figure 5, the crustal discontinuities are much smaller than the those in the overlying crust according to our calculation. In the Tian Shan range, crustal discontinuities are still not evident

except in Aksu, China. The maximum values of THDs in the western Pamir are significant, and the gradient belt extends farther southward into the Hindu Kush area. The material discontinuities near the WHS are mostly limited to the south of the RE (Rushan Pshart suture zone) and widely continuous according to our calculation. The structural discontinuities between the Pamir Plateau and the Tarim basin become indistinct. On the Tibetan Plateau, crustal discontinuities in the Himalayan tectonic zone are more evident than those in northern Tibet. Only the KKF, ATF and QNF exhibit certain extents of structural discontinuities. In addition, the AMS (Anyimaqen-Kunlun-Muztagh suture zone) between the Qaidam basin and the Tibetan Plateau is partly evident according to the maximum values of the THDs. In the Himalayan tectonic zone, the maximum values along the N-S-trending normal faults decrease, except for those in the crust west of the GM and east of the SNF. In eastern Tibet, the crustal discontinuities of the EHS are as evident as those of the WHS. The NjF, BtF (Ba Tang fault) and JsjF are still notable according to the distribution of maximum THD values.

Figure 5. Distributions of the total horizontal derivatives at 6.5 km depth

In Figure 6, the maximum values of the THDs in the Pamir Plateau decrease and vanish. The current depth is close to the crystalline basement of the plateau. This indicates that the crustal materials of the basement are relatively intact. The maximum values of the THDs are mostly distributed over the WHS and SSZ, and the western segment of the PTS exhibits a degree of discontinuity. The distribution of maximum values in the Himalayan tectonic zone is relatively homogeneous, and differences in crustal discontinuities among the western, middle and eastern segments of the Himalayan are not as obvious as those in the overlying crust. The GM and the southern segments of the N-S-trending normal faults, including the ALAF (Alucuo-Lamucuo-Aguocuo fault), CPF (Cangmucuo-Palongcuo fault) and XSDF, which are divided by the MCT, exhibit significant crustal discontinuities. In addition, the southern end of the YGF and its eastern structures, such as the YZYS, SNF and MCT, exhibit evident crustal discontinuities. The THD values along the JlF and AplF near the EHS decrease, and only the frontal great bend of the YZYS exhibits a degree of crustal discontinuity. In eastern Tibet, the maximum values are distributed discretely at almost the same latitude from the NjF in the west to the AnhF in the east. Further, crustal discontinuities in the western crust of the LmsT are obvious.

Figure 6. Distributions of the total horizontal derivatives at 10 km depth

In Figure 7, the crustal discontinuities are mostly concentrated in several separate parts of the boundary zone between the Indian and Eurasian plates. On the Pamir Plateau, the maximum values of the THDs in the E-W direction are mainly distributed in front of the WHS, from the SSZ to the KKS. In the Himalayas, crustal discontinuities are more evident near the KF, southern segments of the ALAP and southern CPF, and they are cut by the MCT and eastern SNF. The distribution of maximum values of the THDs obviously decreases in eastern Tibet. Only very limited discrete maximum values are found near the EHS and the NW segment of the NjF.

Figure 7. Distributions of the total horizontal derivatives at 17 km depth

The spatial distribution characteristics of the THDs at depths of 85 km (Figure 8) and 136 km (Figure 9) are significantly different from those in the overlying crust (as shown in Figure 3-Figure 7) and may correspond to the structural difference between the upper mantle and crust. Such variations can also be indicated by Figure 2. The mean depth of the Mohorovicic discontinuity is 85 km in the study area according to our calculation, which also coincides with the result of Li et

al. (2018). In general, the characteristics of the tectonic discontinuities in the upper mantle are very different from those in the overlying crust. In Figure 8, the maximum values of the THDs are mainly distributed along the eastern and western margins of Tibet. The discontinuity along the HF (Herat fault) and RE in the southern Pamir exhibits leading-edge features of the subducting Indian plate. The discontinuities along the KKF, KF, LGF, ATF and XSDF are still evident at current depths, which indicates that these faults are major fracture structures that cut deep into the lithosphere. Note that the lithospheric materials between the Himalayan tectonic zone and the EHS are obviously separated by the SNF. The maximum values of the THD distribution in eastern Tibet exhibit significant material discontinuities in the EHS. In contrast with Figure 2(g), a continuous high positive gradient belt protrudes into the negative anomalies and separates the negative anomalies into several discrete segments. Such spatial patterns of both the Bouguer gravity anomalies and THD maximum values indicate that the widely distributed structural discontinuities in the EHS could be the result of both fault activity and crustal stacking or folding of the Mohorovicic discontinuity caused by the wedging Indian plate.

Figure 8. Distributions of the total horizontal derivatives at 85 km depth

The source depth in Figure 9 corresponds to the upper mantle in the study area. The spatial distributions of the maximum THD at this depth show a significant difference between the Pamir Plateau and Tibetan Plateau, and the tectonic discontinuities in the Pamir Plateau are much more significant than those in the Tibetan Plateau. In detail, the lithospheric discontinuities of the Pamir Plateau are mainly distributed north of the MFT and extend northeastward to the STT (Southern Tian Shan thrust), KYS and KKF, which form the western boundary of the Tarim basin and indicate the existence of structural discontinuities between the two major tectonic units. Such a pattern of maximum values exhibits the leading-edge characteristics of the subducting Indian plate. In the Tian Shan range, the maximum values of the THDs are mostly distributed west of the TF, which is also revealed by the spatial distribution of the Bouguer gravity anomalies shown in Figure 2(g). In addition, the Tajik-Afghan basin and the Tarim basin are relatively intact compared with the Pamir Plateau. On the Tibetan Plateau, the pattern of maximum values is approximately elliptical; the major axes are consistent with the directions of regional tectonic structures and display evident clockwise rotation near the EHS. The most significant characteristic of eastern Tibet is that the maximum values form a gradient belt that is distributed along the GlgF (Gaoligong fault) and SF (Sagaing fault).

Figure 9. Distributions of the total horizontal derivatives at 136 km depth

4 Discussion

4.1 Active faults and material discontinuities in the crust

According to the model CRUST1.0 (https://igppweb.ucsd.edu/~gabi/crust1.html), the deposit thickness within the Pamir Plateau increases from 3 km in the south to approximately 6.5 km in the north. Therefore, Figure 3-Figure 5 primarily represent the discontinuities within sedimentary rocks of the Pamir Plateau. In Figure 3 and Figure 4, the maximum values of the THDs are mostly concentrated on the west side of the SKF in the Pamir Plateau, which is consistent with the distribution of regional hypocenters. Thus, the maximum values of the THDs in the western Pamir mostly represent crustal fragmentation. In addition, the distribution of maximum values in the western Pamir extends southward even into the Hindu Kush area (Figure 5). We infer that this

fractured crust is related to the gravitational collapse of sedimentary rocks from the western Pamir to the Tajik-Afghan basin, which is consistent with the research of Schurr et al. (2014). The material discontinuities along the PTS, as shown in Figure 3, Figure 5 and Figure 6, can be obviously tracked between the SKF and the Tajik-Afghan basin. Compared with the deeper crust, the crust shallower than 17 km mainly reflects the collision between the Pamir Plateau and Tian Shan range. According to Figure 6 and Figure 7, the basement of the Pamir Plateau is relatively intact since the maximum values of the THDs are mainly distributed along boundary structures such as the PTS, SSZ and WHS, among which the SSZ should be a deep active fault that cuts through the entire lithosphere.

The current activity of the faults can also be inferred from the spatial distribution of the THDs. There are obvious maximum values distributed along the KF when the depth exceeds 0.5 km (Figure 3). This fault is blind at the surface of the Earth according to our calculation. Thus, it could be indicated that the KF is a major fault between the Pamir Plateau and the Tibetan Plateau, but its present-day activity might not be clear enough because its overlying structures are much less affected by its activity. This indication was proven by GPS observations that the slip rate along the KF is less than 5 mm/yr (Jade et al. 2004). The KYS between the Pamir Plateau and the Tarim basin should be a major deep fault that cuts through the entire lithosphere because the material discontinuity along this fault can be recognized in all wavelet details. The RE and KKF are more evident near the bottom of the regional basement, while their discontinuities are not evident in the shallower crust (as shown in Figure 3 and Figure 4). This indicates that their activity is relatively weak at present.

In eastern Tibet, most faults are concentrated within the shallow crust except for the NjF. The discontinuities along the XshF are only revealed at depths below 6.5 km, which indicates that this fault is active (Yan et al. 2018) at present. Most faults in northern Tibet cut deep into the crust, and their influences on the material discontinuities in the upper crust are very limited. The maximum values of the THDs distributed in the Himalayan tectonic zone are mostly consistent with a series of N-S-trending normal faults, and the corresponding discontinuities along these faults are widespread in the crust. This pattern indicates that the E-W extension of southern Tibet is a commonly occurring phenomenon. In addition, the crustal discontinuities over the GM and along the SNF are significant and indicate that these two structures cut through the entire lithosphere. The crustal discontinuities along the WHS are discovered in both the basement and the overlying structures, while those in the EHS are mostly concentrated in the crust at depths below 10 km. Thus, this study reflects distinct characteristics between the WHS and EHS; the crustal deformation in the WHS involves both basement and cover structures, and the deformation in the EHS is relatively shallower.

4.2 Active faults and lithospheric discontinuities in the upper mantle

When depths exceed 85 km, as shown in Figure 8 and Figure 9, the patterns of the THDs are very different from those in the overlying crust. This indicates that the tectonic structures are distinct at the current depth due to the significant structural differences between the overlying crust and the upper mantle. The material discontinuities shown in Figure 8 are mostly related to the structural differences between the lower crust and the upper mantle, where these two distinct tectonic units appear alternately at a depth of 85 km. As discussed in 4.1, crustal discontinuities in the EHS are mostly distributed at depths below 10 km, whereas they become significant again at a depth of 85 km. Such spatial variations with depth in the EHS indicate a relatively complex tectonic structural distribution in which both the Mohorovicic discontinuity and the overlying crust might be strongly deformed by the intense collision between the Indian and Eurasian plates.

Among these faults, the SNF might be another major deep active fault in the study area. This fault forms an obvious tectonic boundary between the Himalayan tectonic zone and the EHS. The maximum values of the THDs at the current depth in the Pamir Plateau are mostly distributed between the RE in the north and the CF and MFT in the south. The CF and MFT are two widely recognized boundaries between the Indian plate and the Eurasian plate, which represent the leading edge of the subducting Indian plate (Figure 8); these boundaries indicate that the frontal area of the Indian plate in the western Himalayas has reached the SW margin of the Tarim basin, which is also proven by a study of seismic wave anomalies published by Li et al. (2008).

In the upper mantle (Figure 9), the distributions of the THD maximum values are significantly different from those in Figure 8. The gradient belts of the THD maximum values are mostly concentrated in the Pamir Plateau, Hindu Kush, Sulaiman Range and WHS and exhibit significant leading-edge tectonic features. Given the contrasts in discontinuities between the EHS and WHS, the collision between the Indian plate and the Eurasian plate is deeper in the west and shallower in the east. The maximum values of the THDs distributed around the WHS reach the boundary of the Tarim basin and form a closed structure in western Tibet. This pattern can help to explain the mechanisms by which the Pamir Plateau and Tarim basin are moving northward at the same rate, which is revealed by GPS observations (Ischuk et al. 2010; Zubovich et al. 2016). Furthermore, the collision zone is closed in the west but open in the east. This supports the basic assumption that the structural closure in the west forms the boundary condition for the eastward tectonic escape of the entire Tibetan Plateau.

5 Conclusions

We studied the spatial distribution characteristics of major active faults and structural discontinuities in the boundary zone between the Indian plate and the Eurasian plate. The wavelet multiscale analysis technique and radial power spectrum algorithm were utilized in this paper to obtain the Bouguer gravity anomalies at different depths. Then, we calculated the THDs to recognize the discontinuities in the lithospheric materials that indicate the existence of major active faults and tectonic boundaries. The main conclusions of our study are as follows.

1) The upper crust of the western Pamir is significantly fragmented, and such fragmentation might be caused by the gravitational collapse of sedimentary rocks from the western Pamir to the Tajik-Afghan basin.

2) The crust at depths of 10 km to 17 km beneath the Pamir Plateau is relatively intact, whereas boundary structures such as the PTS, SSZ and WHS exhibit significant structural discontinuities. Among these faults, the SSZ is a deep active fault that cuts through the entire lithosphere. In addition, the PTS is mostly exposed to depths below 17 km. This result indicates that the collision between the Pamir Plateau and the southern Tian Shan might occur in the upper crust.

3) In the Himalayan tectonic zone, the discontinuities along a series of N-S-trending normal faults as well as the GM are more evident than other structures, and the Himalayan crust is under evident E-W extension over a relatively wide range of depths. The SNF is another major fault that cuts through the entire lithosphere and forms the tectonic boundary between the EHS and the Himalayan tectonic zone in the upper mantle.

4) The characteristics of spatial structural distributions are very different between the WHS and the EHS. On the one hand, the former penetrates deeper into the lithosphere than the latter. On the other hand, the structure of the former is relatively intact and can be clearly recognized in both the upper mantle and the overlying crust, whereas the latter is more complex; the crust and the

Mohorovicic discontinuity are both undergoing intense deformation due to the collision between the Indian and Eurasian plates.

5) The leading edge of the subducting Indian plate in the upper mantle reaches the SW boundary of the Tarim basin and forms a closed structure in the west, which may help to explain the eastward tectonic escape of the Tibetan Plateau.

Acknowledgments, Samples, and Data

We are grateful to the UCSD for providing Free-air gravity anomaly data. We also appreciate J. Fullea(Group of Dynamics of the Lithpsphere, Instituto de Ciencias de la Tierra (Jaume Almera), CSIC 08028 Barcelona, Spain) with sharing their Fortran 90 code to compute Bouguer gravity anomalies . This work was supported by the National Natural Science Foundation of China (NSFC) Project (Grant No. 41701069) and 2019 Special Scientific Research Plan of the Education Department of Shaanxi Province(Grant No. 19JK0523).

Data availability statement. The gravity field analyzed during this research are available in the Scripps Institution of Oceanography, University of California San Diego, https://topex.ucsd.edu/index.html.

References

Ansberque, C., Godard, V., Olivetti, V., Bellier, O., De Sigoyer, J., Bernet, M., ... & Ehlers, T. A. (2018) Differential Exhumation Across the Longriba Fault System: Implications for the Eastern Tibetan Plateau. *Tectonics*, 37(2), 663-679. doi:10.1002/2017TC004816

Bhatti, Z. I., Zhao, J., Khan, N. G., & Shah, S. T. (2018) Structure of crust and upper mantle beneath NW Himalayas, Pamir and Hindukush by multi-scale double-difference seismic tomography. *Physics of the Earth and Planetary Interiors*, 281, 92-102. doi:10.1016/j.pepi.2018.06.001

Burtman, Valentin & Molnar, Peter. (1993) Geological and Geophysical Evidence for Deep Subduction of Continental Crust Beneath the Pamir. *Spec. Paper Geol. Soc. Am.*. 281. doi: 10.1130/SPE281-p1

Burtman, V. S. (2013) The geodynamics of the Pamir-Punjab syntaxis. *Geotectonics*, 47(1), 31–51. doi:10.1134/S0016852113010020

Chen, W., & Yang, Z. (2004) Earthquakes Beneath the Himalayas and Tibet: Evidence for Strong Lithospheric Mantle. *Science*, 304(5679), 1949-1952. doi: 10.1126/science.1097324

Chung, S., Lee, T. Y., Lo, C., Wang, P., Chen, C., Yem, N. T., ... & Genyao, W. (1997) Intraplate extension prior to continental extrusion along the Ailao Shan-Red River shear zone. *Geology,* 25(4), 311-314. doi:10.1130/0091-7613 (1997) 025 <0311:IEPTCE> 2.3.CO;2

Deng Q D, Ran Y K, Yang X P,et al.(2007) Active tectonics map of China(in Chinese). *Beijing: Seismological Press.*

Dong P Y, Shi Y L, Cheng H H, et al. (2020) Numerical analysis of the future seismic hazards in the Tibetan Plateau and its surrounding area. *Chinese J. Geophys. (in Chinese)*, 63(3), 1155-1169. doi: 10.6038/cjg2020N0310

England, P., & Mckenzie, D. (1982) A thin viscous sheet model for continental deformation. *Geophysical Journal International*, 70(2), 295-321. doi:10.1111/j.1365-246X.1982.tb04969.x

England, P., & Houseman, G. A. (1986) Finite strain calculations of continental deformation: 2. Comparison with the India-Asia Collision Zone. *Journal of Geophysical Research*, 3664-3676. doi:10.1029/JB091iB03p03664

England, P., & Molnar, P. (1990) Right-lateral shear and rotation as the explanation for strike-slip faulting in eastern Tibet. *Nature*, 344(6262), 140-142. doi: 10.1038/344140a0

Fullea, J., Fernindez, M., & Zeyen, H. (2008) FA2BOUG-A FORTRAN 90 code to compute Bouguer gravity anomalies from gridded free-air anomalies: Application to the Atlantic-Mediterranean transition zone. *Computers & Geosciences*, 34(12), 1665-1681. doi: 10.1016/j.cageo.2008.02.018

Gao Y, Shi Y T, Wang Q. (2020) Seismic anisotropy in the southeastern margin of the Tibetan Plateau and its deep tectonic significances. *Chinese J. Geophys. (in Chinese)*, 63(3):802-816, doi: 10.6038/cjg2020O0033

Ge, W., Molnar, P., Shen, Z., & Li, Q.(2015) Present-day crustal thinning in the southern and northern Tibetan Plateau revealed by GPS measurements. *Geophysical Research Letters*, 42(13), 5227-5235. doi: 10.1002/2015GL064347

Houseman, G. A., & England, P. (1986) Finite strain calculations of continental deformation: 1. Method and general results for convergent zones. *Journal of Geophysical Research*, 3651-3663. doi: 10.1029/JB091iB03p03651

Hardy R L. (1978) The application of multiquadric equations and point mass anomaly models to crustal movement studies. Department of Commerce, National Oceanic and Atmospheric Administration, National Ocean Survey, National Geodetic Survey.

Holt, W. E., Li, M., & Haines, A. J. (1995) Earthquake strain rates and instantaneous relative motions within central and eastern Asia. *Geophysical Journal International*, 122(2), 569-593. doi: 10.1111/j.1365-246X.1995.tb07014.x

Holt, W. E., Chamotrooke, N., Pichon, X. L., Haines, A. J., Shentu, B., & Ren, J. (2000) Velocity field in Asia inferred from Quaternary fault slip rates and Global Positioning System observations. *Journal of Geophysical Research*, 19185-19209. doi: 10.1029/2000JB900045

Houseman, G. A., & England, P. (1993) Crustal thickening versus lateral expulsion in the Indian-Asian continental collision. *Journal of Geophysical Research*, 12233-12249. doi: 10.1029/93JB00443

Ischuk, A., Bendick, R., Rybin, A. K., Molnar, P., Khan, S. F., Kuzikov, S. I., ... & Zubovich, A. V.(2013) Kinematics of the Pamir and Hindu Kush regions from GPS geodesy. *Journal of Geophysical Research*, 118(5), 2408-2416. doi: 10.1002/jgrb.50185

Jade S, Bhatt B C, Yang Z, et al. (2004) GPS measurements from the Ladakh Himalaya, India: Preliminary tests of plate-like or continuous deformation in Tibet. *Geological Society of America Bulletin*, 116(11-12): 1385-1391. doi: 10.1130/B25357.1

Li, C., Der Hilst, R. D., Meltzer, A., & Engdahl, E. R. (2008) Subduction of the Indian lithosphere beneath the Tibetan Plateau and Burma. *Earth and Planetary Science Letters*, 274(1), 157-168. doi:10.1016/j.epsl.2008.07.016

Li Q S, Gao Y, Wang X B et al. (2020) New research progress in geophysics and continental dynamics of the Tibetan Plateau. *Chine J. Geophys. (in Chinese)*, 63(3): 789-801. doi:10.6038/cjg2020O0063

Li, Y., Liu, M., Wang, Q., & Cui, D. (2018) Present-day crustal deformation and strain transfer in northeastern Tibetan Plateau. *Earth and Planetary Science Letters*, 179-189. doi: 10.1016/j.epsl.2018.01.024

Li W , Xu C , Yi L , et al. (2019) Source parameters and seismogenic structure of the 2017 Mw 6.5 Mainling earthquake in the Eastern Himalayan Syntaxis (Tibet, China), *Journal of Asian earth sciences*, 169(JAN.):130-138. doi: 10.1016/j.jseaes.2018.07.027.

Liang, S., Gan, W., Shen, C., Xiao, G., Liu, J., Chen, W., ... & Zhou, D. (2013) Three-dimensional velocity field of present-day crustal motion of the Tibetan Plateau derived from GPS measurements. *Journal of Geophysical Research*, 118(10), 5722-5732. doi: 10.1002/2013JB010503

Molnar, P., & Tapponnier, P. (1975) Cenozoic Tectonics of Asia: Effects of a Continental Collision: Features of recent continental tectonics in Asia can be interpreted as results of the India-Eurasia collision. *Science*, 189(4201), 419-426. doi: 10.1126/science.189.4201.419

Molnar, P., & Qidong, D. (1984) Faulting associated with large earthquakes and the average rate of deformation in central and eastern Asia. *Journal of Geophysical Research*, 6203-6227. doi:10.1029/JB089iB07p06203

Pan, Z., He, J., & Li, J. (2018) Contemporary Crustal Deformation Within the Pamir Plateau Constrained by Geodetic Observations and Focal Mechanism Solutions. *Pure and Applied Geophysics*, 175(10), 3463-3484. doi:10.1007/s00024-018-1872-3

Sandwell, D. T., Muller, R. D., Smith, W. H., Garcia, E. S., & Francis, R. (2014) New global marine gravity model from CryoSat-2 and Jason-1 reveals buried tectonic structure. *Science*, 346(6205), 65-67. doi:10.1126/science.1258213

Schurr, B., Ratschbacher, L., Sippl, C., Gloaguen, R., Yuan, X., & Mechie, J. (2014) Seismotectonics of the Pamir. Tectonics, 33(8), 1501-1518. doi:10.1002/2014TC003576

Schwab, M., Ratschbacher, L., Siebel, W., Mcwilliams, M., Minaev, V., Lutkov, V., ... & Wooden, J. L. (2004) Assembly of the Pamirs: Age and origin of magmatic belts from the southern Tien Shan to the southern Pamirs and their relation to Tibet. *Tectonics*, 23(4). doi:10.1029/2003TC001583

Taylor, M. H., & Yin, A. (2009) Active structures of the Himalayan-Tibetan orogen and their relationships to earthquake distribution, contemporary strain field, and Cenozoic volcanism. *Geosphere*, 5(3), 199-214. doi: 10.1130/GES00217.1

Tapponnier, P., Peltzer, G., Dain, A. Y., Armijo, R., & Cobbold, P. R. (1982) Propagating extrusion tectonics in Asia: New insights from simple experiments with plasticine. *Geology*, 10(12), 611-616. doi: 10.1130/0091-7613(1982)10<611:PETIAN>2.0.CO;2

Vilotte, J., Daignieres, M., & Madariaga, R. (1982) Numerical modeling of intraplate deformation: Simple mechanical models of continental collision. *Journal of Geophysical Research*, 10709-10728. doi:10.1029/JB087iB13p10709

Wang, Q., Zhang, P., Freymueller, J. T., Bilham, R., Larson, K. M., Lai, X., ... & Chen, Q. (2001) Present-day crustal deformation in China constrained by global positioning system measurements.*Science*, 294(5542), 574-577. doi: 10.1126/science.1063647

Wang, W., Pan, Y., & Qiu, Z. (2009) A new edge recognition technology based on the normalized vertical derivative of the total horizontal derivative for potential field data. *Applied Geophysics*, 6(3), 226-233. doi: 10.1007/s11770-009-0026-x

Wu X L, Xiang Y, Tang F Q. (2020) Study on current crustal deformation of the Himalayan tectonic zone by GPS strain-rate estimation and focal mechanism stress inversion. *Chinese J. Geophys. (in Chinese)*, 63(8): 2924-2939. doi: 10.6038/cjg2020N0362

Xu, C., Wang, H., Luo, Z., Ning, J., & Liu, H. (2015) Multilayer stress from gravity and its tectonic implications in urban active fault zone: A case study in Shenzhen, South China. *Journal of Applied Geophysics*, 174-182. doi: 10.1016/j.jappgeo.2015.01.017

Yan, B., Toda, S., & Lin, A. (2018) Coulomb Stress Evolution History as Implication on the Pattern of Strong Earthquakes along the Xianshuihe-Xiaojiang Fault System, China. *Journal of Earth Science*, 29(2), 427-440. doi: 10.1007/s12583-018-0840-2

Yang W C, Jin S, Zhang L L, et al. (2020) The three-dimensional resistivity structures of the lithosphere beneath the Qinghai Tibet Plateau. *Chinese J. Geophys. (in Chinese)*, 63(3): 817-827. doi: 10.6038/cjg2020N0197

Yang, W., Shi, Z., & Hou, Z. (2001) Discrete wavelet transform for multiple decomposition of gravity anomalies. *Chinese J. Geophys. (in Chinese)*, 44(4), 529-537. doi: 10.1002/cjg2.171

Zhang Y S, Zheng X J, Wang L M. (2016) The distribution characteristics of deformation field caused by three great earthquakes in the Qinghai-Tibet Plateau and its vicinity since 2001. *Chinese J. Geophys. (in Chinese)*, 59(10): 3637-3645, doi: 10.6038/cjg20161011.

Zubovich, A., Schone, T., Metzger, S., Mosienko, O., Mukhamediev, S., Sharshebaev, A., & Zech, C. (2016) Tectonic interaction between the Pamir and Tien Shan observed by GPS. *Tectonics*, 35(2), 283-292. doi: 10.1002/2015TC004055.

Figure1.

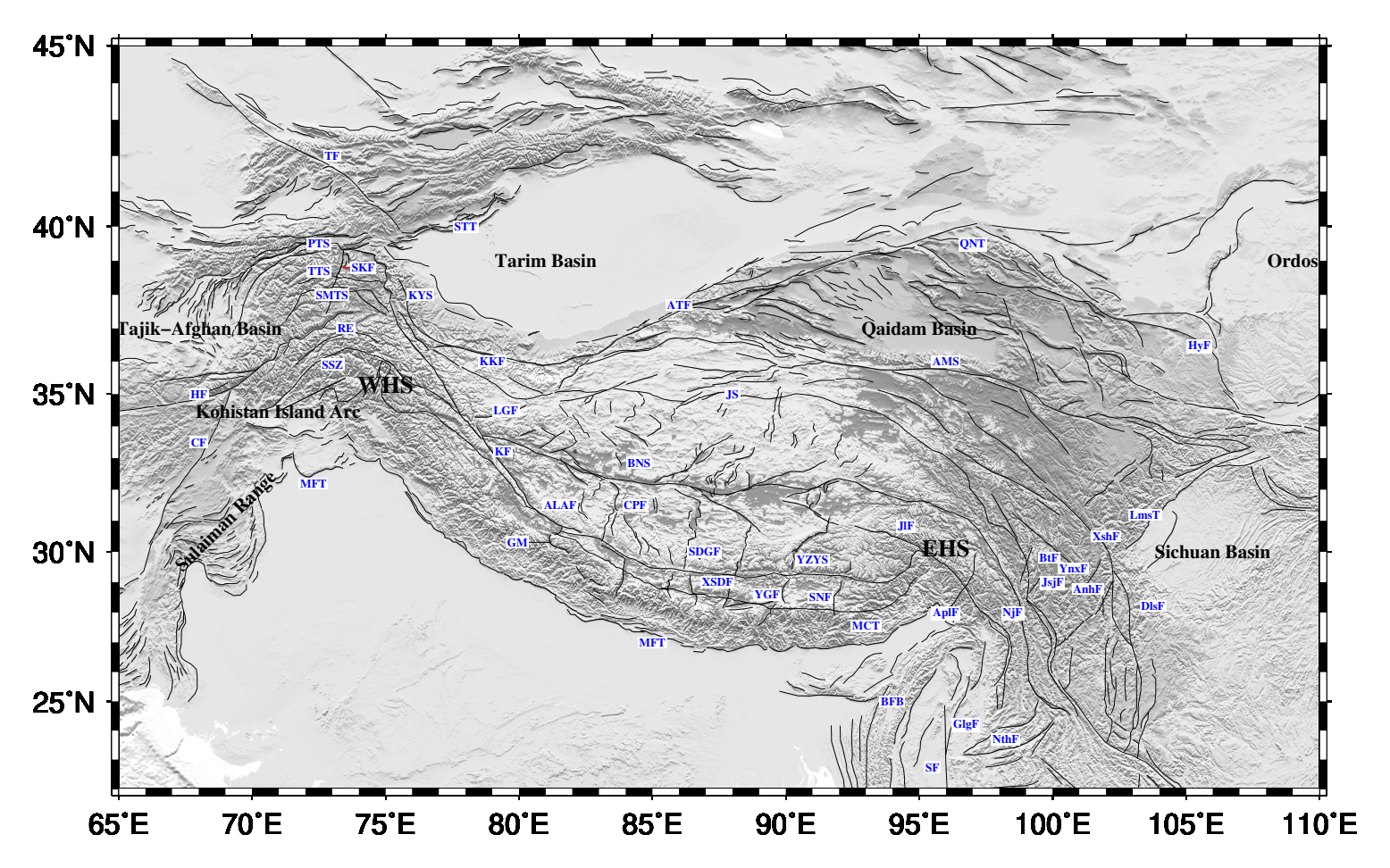
45°N
40°N
35°N
30°N
25°N
65°E
70°E
75°E
80°E
85°E
90°E
95°E
100°E
105°E
110°E
TF
STT
PTS
TTS
SKF
SMTS
KYS
RE
SSZ
HF
CF
MFT
KKF
LGF
KF
BNS
ALAF
CPF
GM
SDGF
XSDF
YGF
SNF
YZYS
JIF
MCT
MFT
ATF
QNT
AMS
JS
HyF
LmsT
XshF
BtF
YnxF
JsjF
AnhF
DlsF
NjF
AplF
BFB
GlgF
NthF
SF
Tarim Basin
Qaidam Basin
Ordos
Tajik–Afghan Basin
WHS
Kohistan Island Arc
Suliaiman Range
EHS
Sichuan Basin

Figure2.

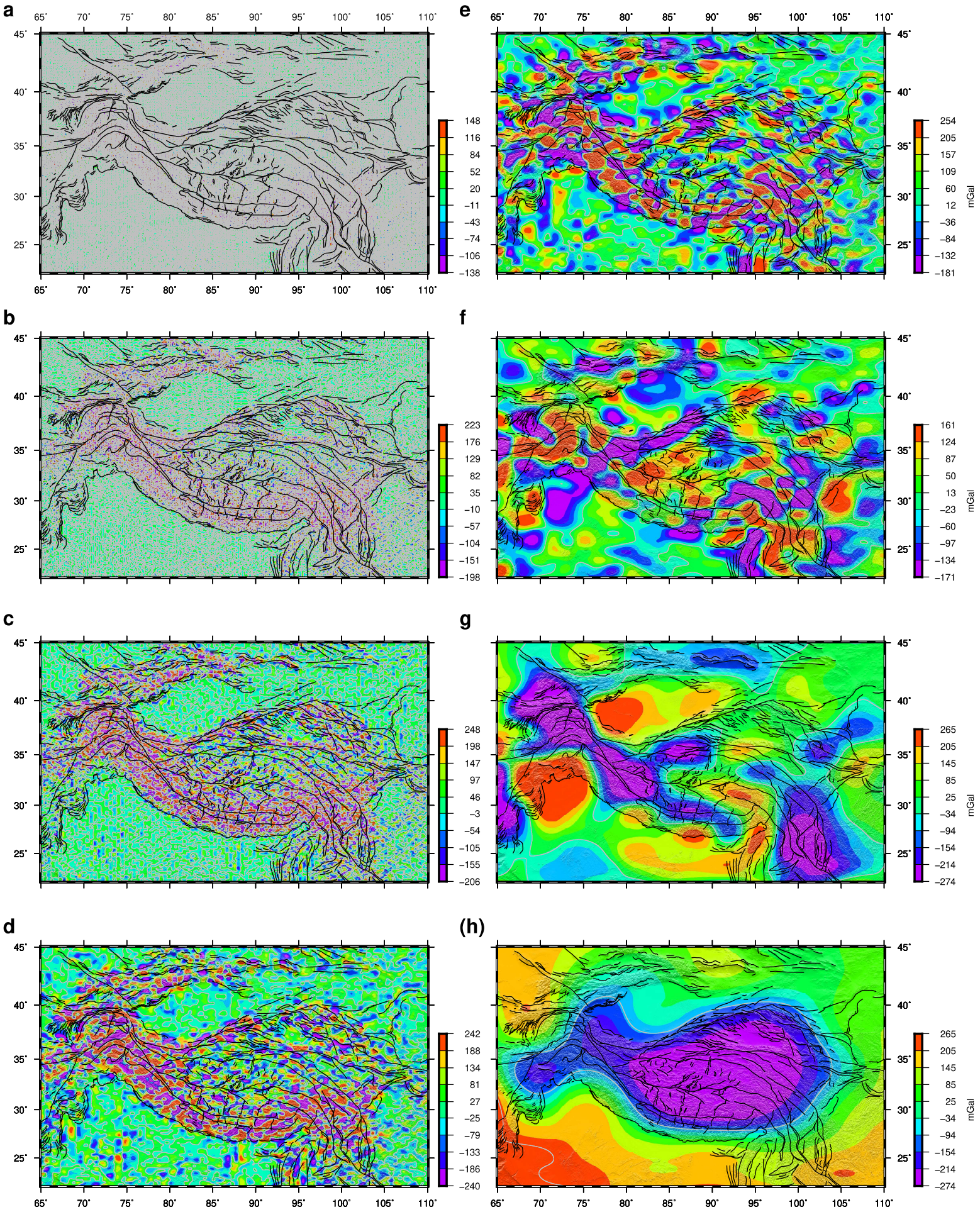
a
b
c
d
e
f
g
(h)
65°
70°
75°
80°
85°
90°
95°
100°
105°
110°
45°
40°
35°
30°
25°
148
116
84
52
20
−11
−43
−74
−106
−138
223
176
129
82
35
−10
−57
−104
−151
−198
248
198
147
97
46
−3
−54
−105
−155
−206
242
188
134
81
27
−25
−79
−133
−186
−240
254
205
157
109
60
12
−36
−84
−132
−181
161
124
87
50
13
−23
−60
−97
−134
−171
265
205
145
85
25
−34
−94
−154
−214
−274
mGal

Figure3.

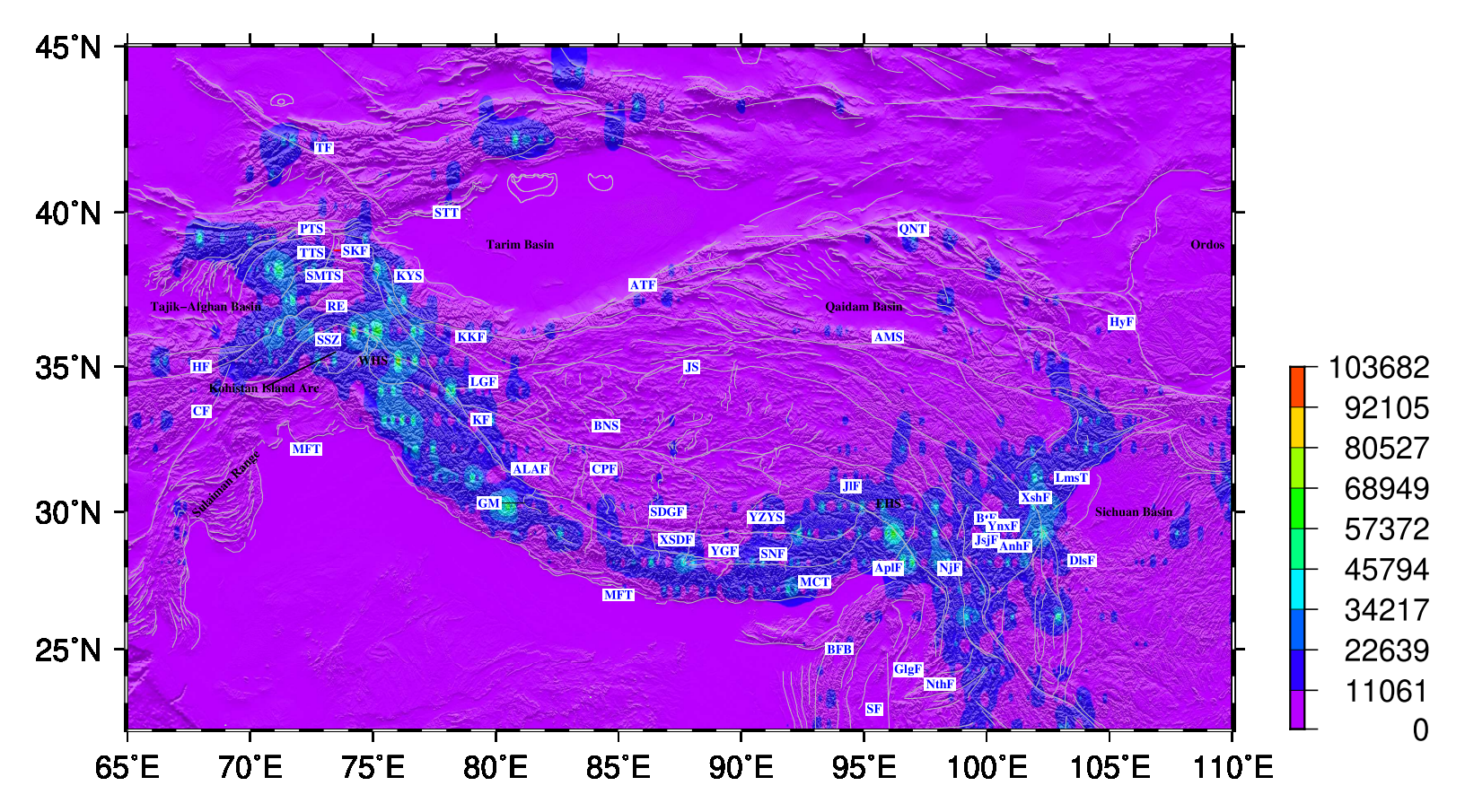
45°N
40°N
35°N
30°N
25°N
65°E
70°E
75°E
80°E
85°E
90°E
95°E
100°E
105°E
110°E
TF
STT
PTS
TTS
SKF
SMTS
KYS
RE
SSZ
KKF
HF
WBS
LGF
CF
KF
MFT
ALAF
CPF
BNS
GM
JS
ATF
QNT
Tarim Basin
Ordos
Tajik–Afghan Basin
Qaidam Basin
HyF
AMS
Kohistan Island Arc
Sulaiman Range
SDGF
YZYS
XSDF
YGF
SNF
MCT
MFT
JIF
EDS
LmsT
XshF
Sichuan Basin
BxF
YnxF
JsjF
AnhF
DlsF
ApIF
NjF
BFB
GlgF
NthF
SF
103682
92105
80527
68949
57372
45794
34217
22639
11061
0

Figure4.

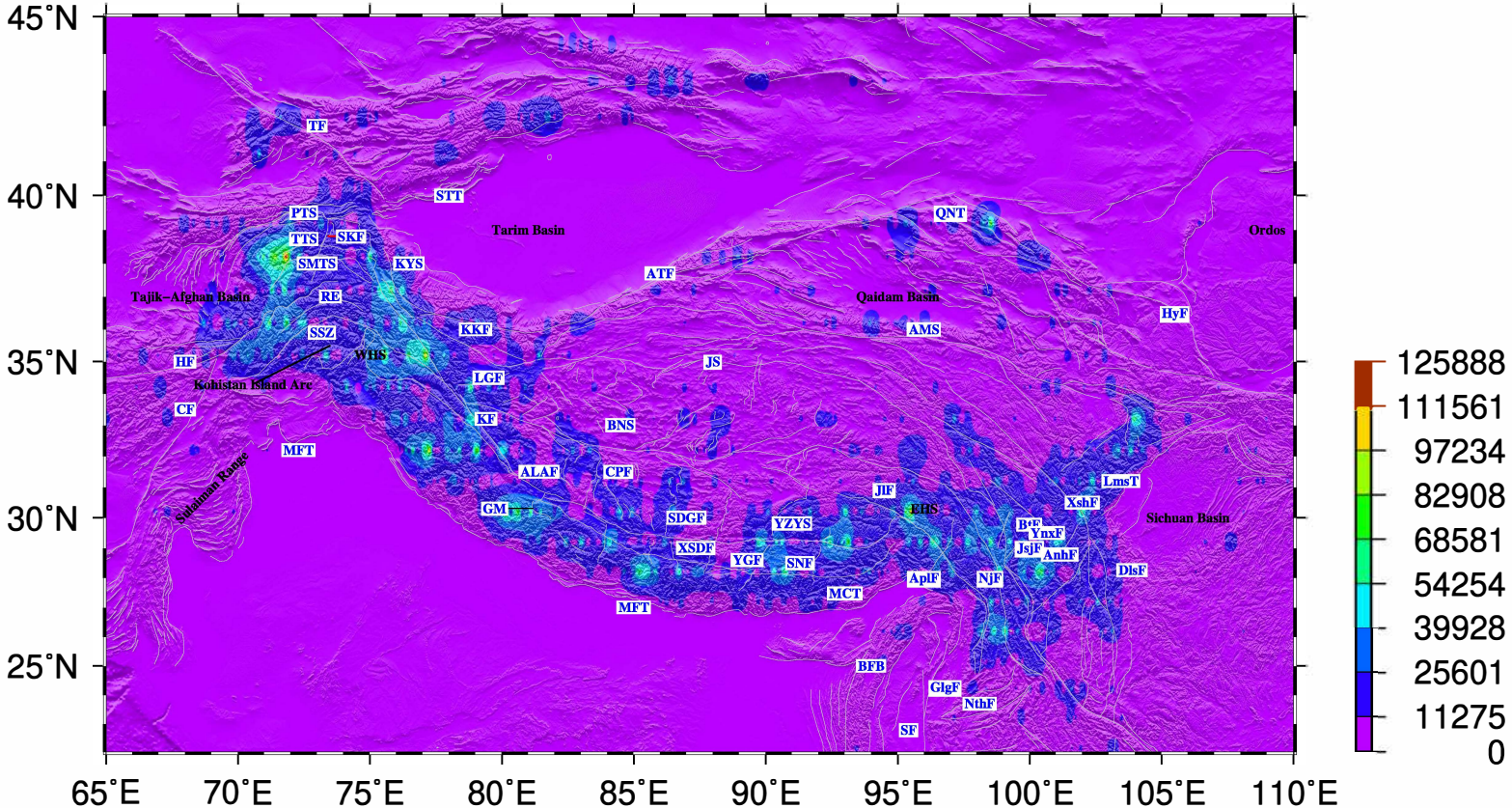
45°N
40°N
35°N
30°N
25°N
65°E
70°E
75°E
80°E
85°E
90°E
95°E
100°E
105°E
110°E
TF
STT
PTS
TTS
SKF
SMTS
KYS
RE
SSZ
HF
WHS
Kohistan Island Arc
CF
MFT
Sulaiman Range
Tarim Basin
Tajik–Afghan Basin
ATF
KKF
LGF
KF
BNS
ALAF
CPF
GM
SDGF
XSDF
YGF
SNF
YZYS
MCT
MFT
JS
QNT
Ordos
Qaidam Basin
AMS
HyF
JIF
EHS
LmsT
XshF
Sichuan Basin
BrF
YnxF
JsjF
AnhF
DlsF
ApiF
NjF
BFB
GlgF
NthF
SF
125888
111561
97234
82908
68581
54254
39928
25601
11275
0

Figure5.

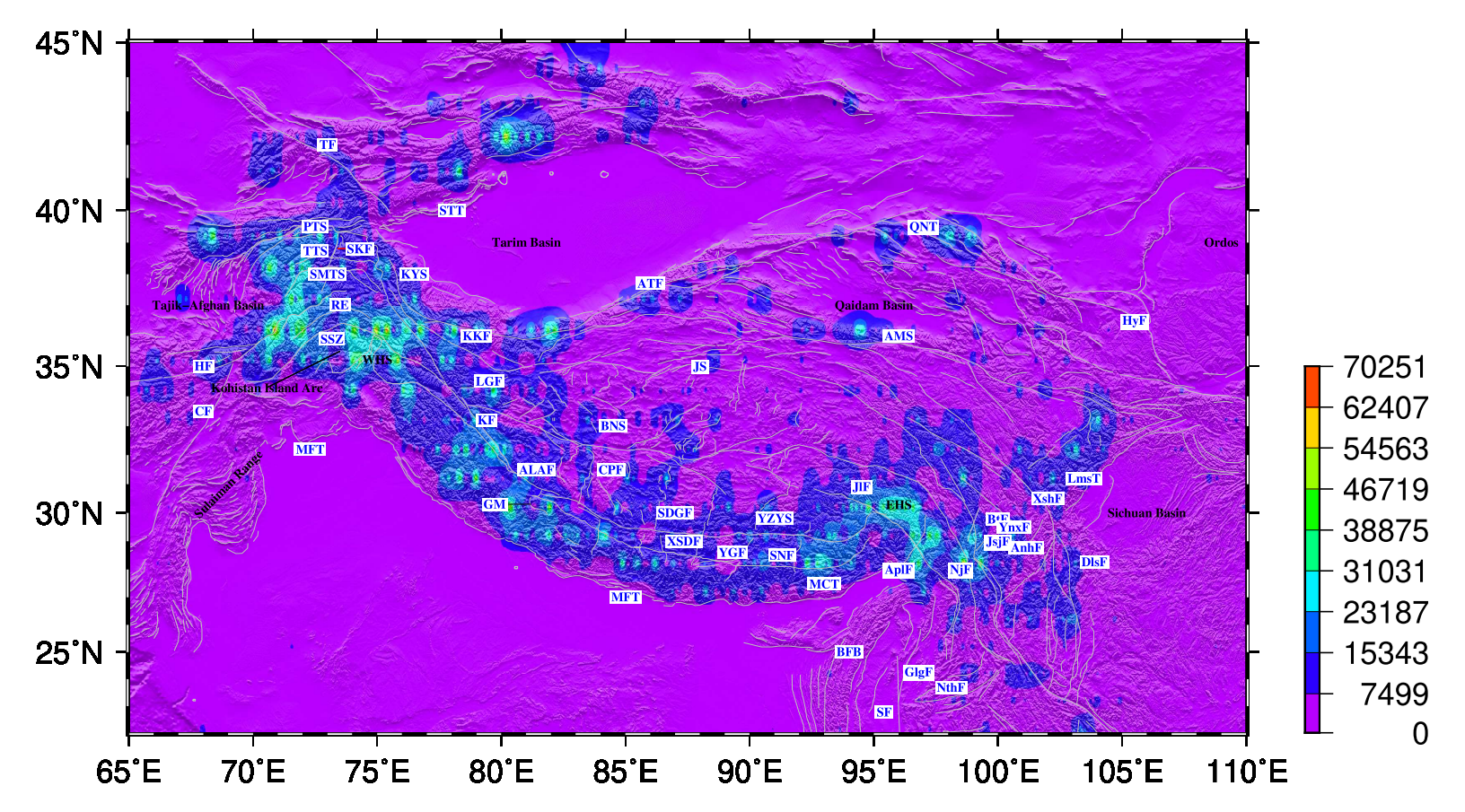
45°N
40°N
35°N
30°N
25°N
65°E
70°E
75°E
80°E
85°E
90°E
95°E
100°E
105°E
110°E
TF
STT
PTS
TTS
SKF
SMTS
KYS
Tarim Basin
ATF
QNT
Ordos
Tajik–Afghan Basin
RE
Qaidam Basin
HyF
SSZ
KKF
AMS
HF
WHS
JS
LGF
Kohistan Island Arc
CF
KF
BNS
MFT
Sulaiman Range
ALAF
CPF
JlF
LmsT
XshF
GM
EHS
Sichuan Basin
SDGF
YZYS
BoF
YnxF
XSDF
JsjF
AnhF
YGF
SNF
DlsF
AplF
NjF
MCT
MFT
BFB
GlgF
NthF
SF
70251
62407
54563
46719
38875
31031
23187
15343
7499
0

Figure6.

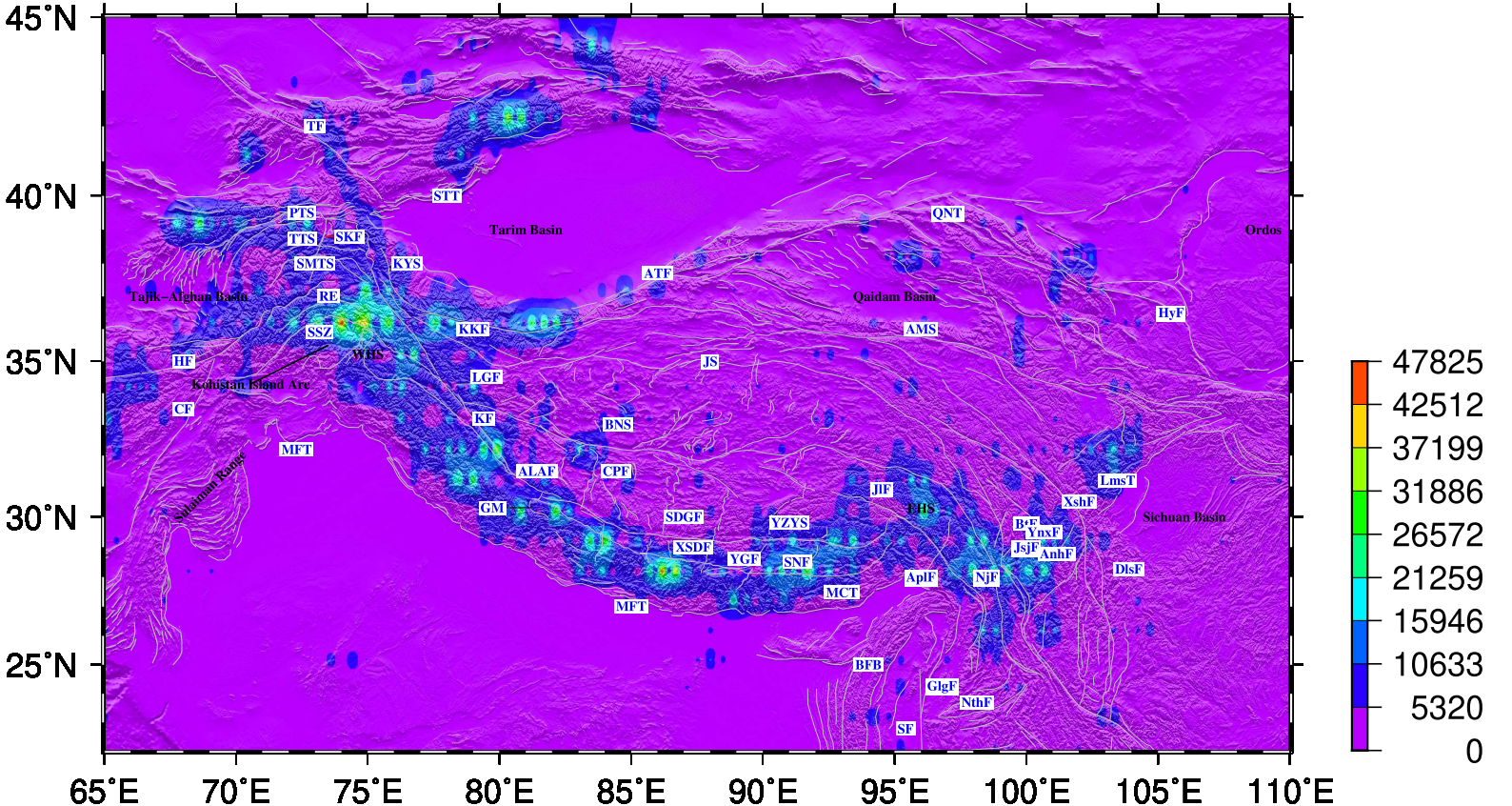
45°N
40°N
35°N
30°N
25°N
65°E
70°E
75°E
80°E
85°E
90°E
95°E
100°E
105°E
110°E
TF
STT
PTS
TTS
SKF
SMTS
KYS
RE
SSZ
KKF
WHS
HF
LGF
CF
KF
BNS
MFT
ALAF
CPF
GM
SDGF
XSDF
YGF
SNF
YZYS
MCT
MFT
BFB
SF
JIF
LHS
AplF
NjF
QNT
ATF
AMS
JS
HyF
LmsT
XshF
BxF
YnxF
JsjF
AnhF
DlsF
GlgF
NthF
Tarim Basin
Qaidam Basin
Ordos
Sichuan Basin
Tajik–Afghan Basin
Kohistan Island Arc
Suleiman Range
47825
42512
37199
31886
26572
21259
15946
10633
5320
0

Figure7.

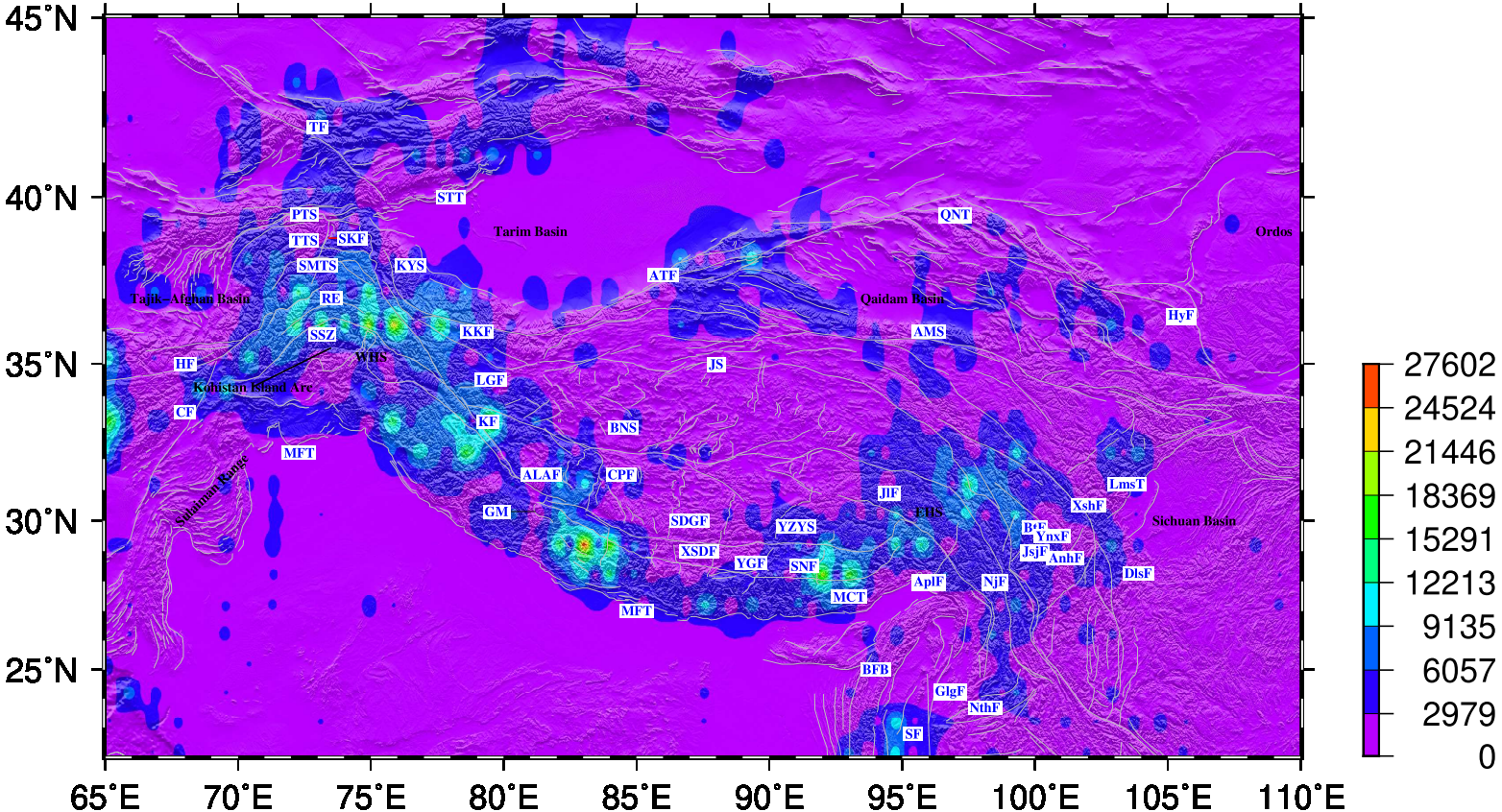
45°N
40°N
35°N
30°N
25°N
65°E
70°E
75°E
80°E
85°E
90°E
95°E
100°E
105°E
110°E
TF
STT
PTS
TTS
SKF
SMTS
KYS
RE
SSZ
KKF
HF
WHS
LGF
CF
KF
MFT
ALAF
CPF
BNS
GM
SDGF
YZYS
XSDF
YGF
SNF
MCT
MFT
BFB
GlgF
NthF
SF
QNT
ATF
AMS
JS
JlF
EHS
BqF
YnxF
JsjF
AnhF
AplF
NjF
DlsF
LmsT
XshF
HyF
Tarim Basin
Qaidam Basin
Ordos
Sichuan Basin
Tajik–Afghan Basin
Kohistan Island Arc
Sulaiman Range
27602
24524
21446
18369
15291
12213
9135
6057
2979
0

Figure8.

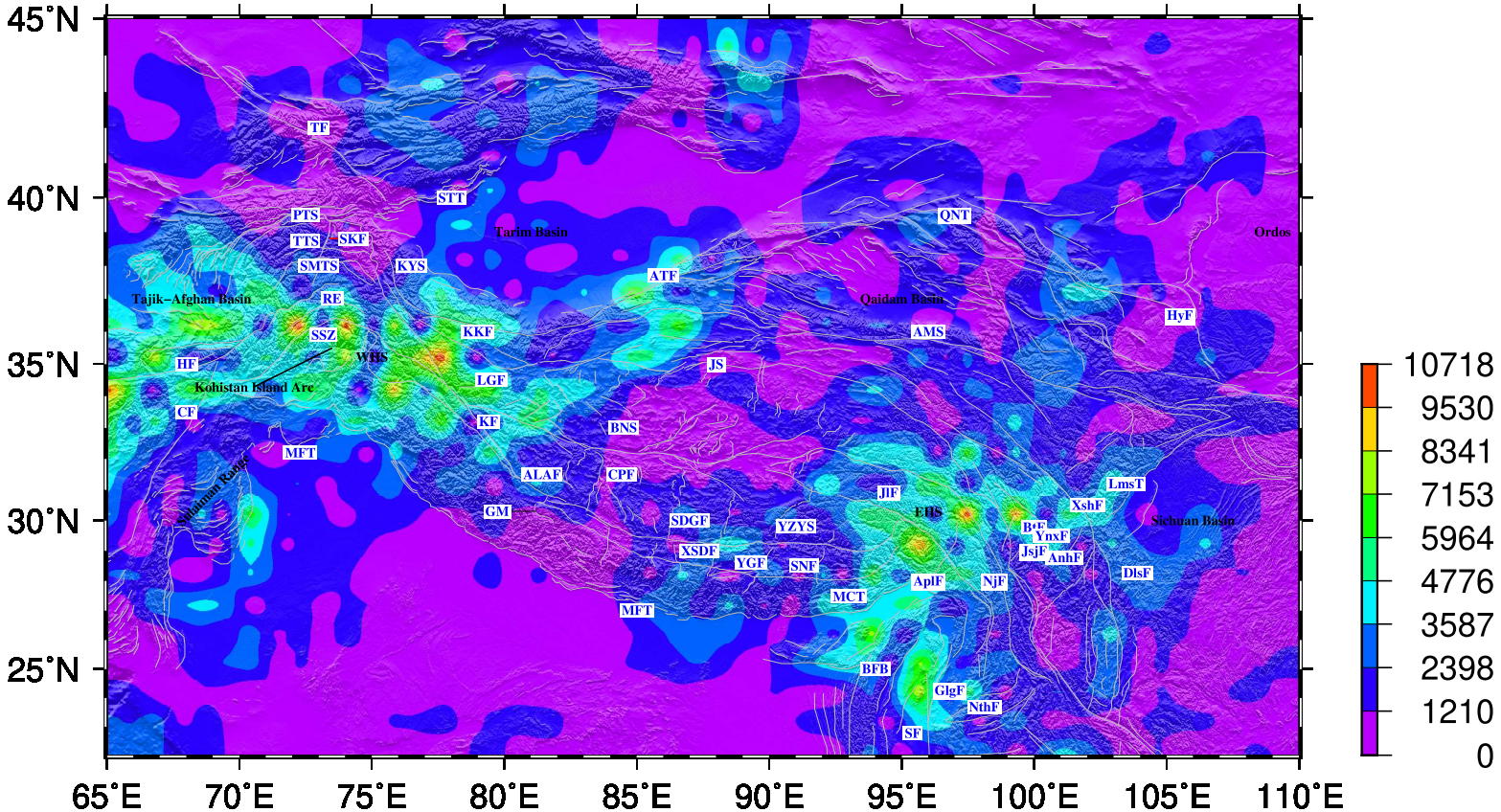
45°N
40°N
35°N
30°N
25°N
65°E
70°E
75°E
80°E
85°E
90°E
95°E
100°E
105°E
110°E
TF
STT
PTS
TTS
SKF
SMTS
KYS
RE
SSZ
WHS
HF
CF
KKF
LGF
KF
BNS
ALAF
CPF
GM
MFT
ATF
JS
SDGF
YZYS
XSDF
YGF
SNF
MCT
MFT
BFB
SF
QNT
AMS
HyF
JIF
EHS
LmsT
XshF
BgF
YnxF
JsjF
AnhF
DlsF
AplF
NjF
GlgF
NthF
Tarim Basin
Tajik–Afghan Basin
Kohistan Island Arc
Sulaiman Range
Qaidam Basin
Ordos
Sichuan Basin
10718
9530
8341
7153
5964
4776
3587
2398
1210
0

Figure9.

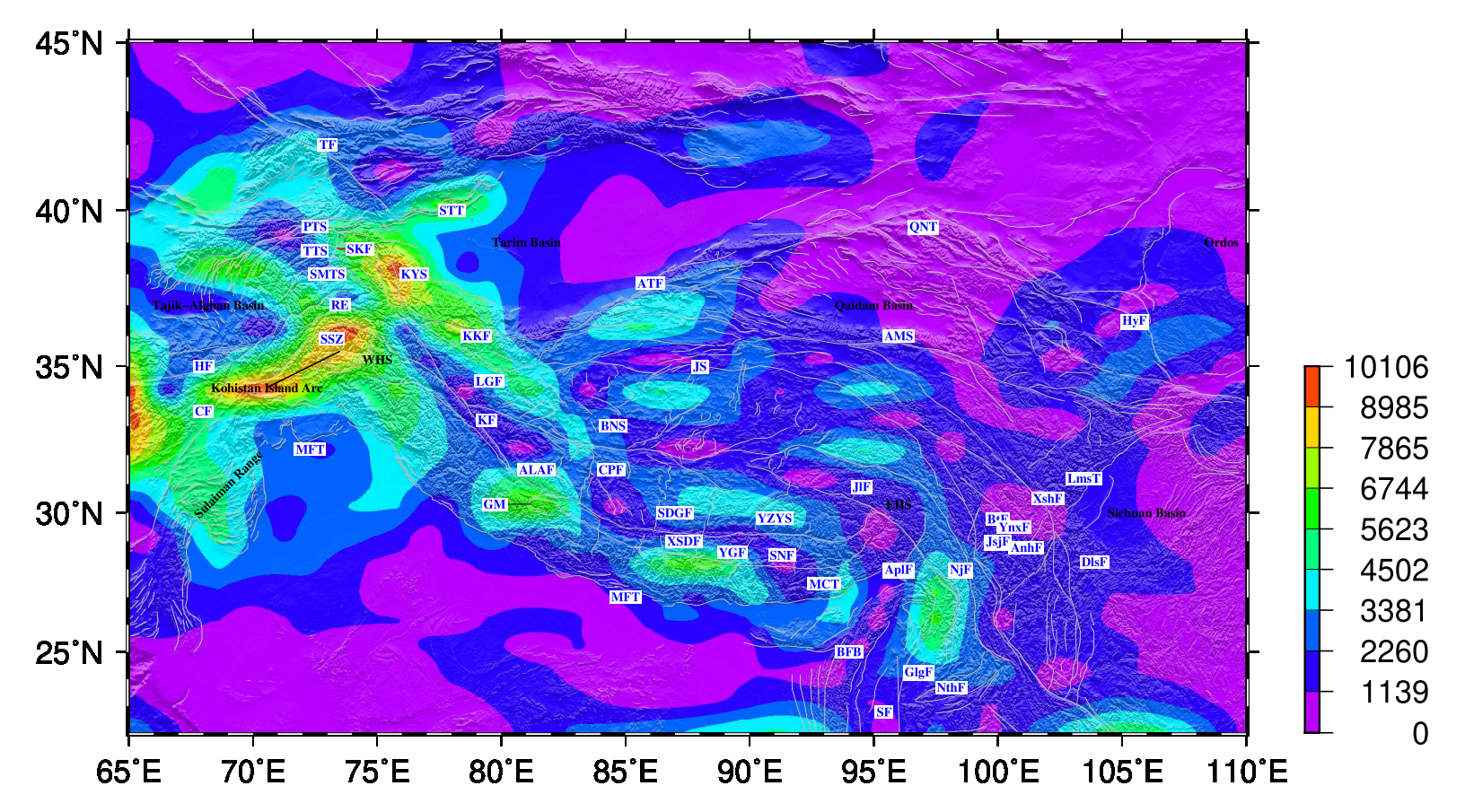
45°N
40°N
35°N
30°N
25°N
65°E
70°E
75°E
80°E
85°E
90°E
95°E
100°E
105°E
110°E
TF
STT
PTS
TTS
SKF
SMTS
KYS
RE
SSZ
WHS
HF
Kohistan Island Arc
CF
KKF
LGF
KF
BNS
MFT
ALAF
CPF
GM
Suleiman Range
Tajik–Afghan Basin
Tarim Basin
ATF
JS
SDGF
XSDF
YGF
SNF
YZYS
MCT
MFT
BFB
SF
QNT
Qaidam Basin
AMS
Ordos
HyF
LmsT
XshF
YnxF
AnhF
DlsF
Sichuan Basin
JiF
LHS
JsjF
AplF
NjF
GlgF
NthF
10106
8985
7865
6744
5623
4502
3381
2260
1139
0